On the influence of the Bay of Bengal's sea surface temperature gradients on rainfall of the South Asian monsoon

Peter MF Sheehan,[a] Adrian J Matthews,[a,b] Benjamin GM Webber,[a,c]
Alejandra Sanchez-Franks,[d] Nicholas P Klingaman,[e] and PN Vinayachandran[f]

[a] Centre for Oceanic and Atmospheric Science, School of Environmental Sciences, University of East Anglia, Norwich, United Kingdom
[b] School of Mathematics, University of East Anglia, Norwich, United Kingdom
[c] Climactic Research Unit, School of Environmental Sciences, University of East Anglia, Norwich, United Kingdom
[d] National Oceanography Centre, Southampton, United Kingdom
[e] National Centre for Atmospheric Science: Climate, and Department of Meteorology, University of Reading, Reading, United Kingdom
[f] Centre for Atmospheric and Oceanic Sciences, Indian Institute of Science, Bangalore, India

ABSTRACT: The southwest monsoon delivers over 70% of India's annual rainfall and is crucial to the success of agriculture across much of South Asia. Monsoon precipitation is known to be sensitive to sea surface temperature (SST) in the Bay of Bengal (BoB). Here, we use a configuration of the Unified Model of the UK Met Office coupled to an ocean mixed layer model to investigate the role of upper-ocean features in the BoB on southwest monsoon precipitation. We focus on the pronounced zonal and meridional SST gradients characteristic of the BoB; the zonal gradient in particular has an as-yet unknown effect on monsoon rainfall. We find that the zonal SST gradient is responsible for a 50% decrease in rainfall over the southern BoB (approximately 5 mm day^{-1}), and a 50% increase in rainfall over Bangladesh and northern India (approximately 1 mm day^{-1}). This increase is remotely forced by a strengthening of the monsoon Hadley circulation. The meridional SST gradient acts to decrease precipitation over the BoB itself, similarly to the zonal SST gradient, but does not have comparable effects over land. The impacts of barrier layers and high-salinity sub-surface water are also investigated, but neither has significant effects on monsoon precipitation in this model; the influence of barrier layers on precipitation is felt in the months after the southwest monsoon. Models should accurately represent oceanic processes that directly influence BoB SST, such as the BoB cold pool, in order to faithfully represent monsoon rainfall.

1. Introduction

The southwest monsoon, which lasts from June to September, delivers over 70% of India's annual rainfall and is crucial to agriculture across South Asia (Parthasarathy et al. 1994; Gadgil and Rupa Kumar 2006). Crops grown during and after the southwest monsoon are strongly affected by the intensity and distribution of its rainfall (Krishna Kumar et al. 2004). Prediction of rainfall at all timescales is of clear importance to the success of each year's harvest and to the prediction of high-impact events such as floods and heat waves (Zhou et al. 2019). Much effort has been put into improving predictions of the southwest monsoon (Bombardi et al. 2020), but seasonal prediction remains particularly challenging, not least because the prevalence of intra-seasonal variability sets the South Asian monsoon system apart from other monsoon systems (Saha et al. 2019). Shortcomings in our understanding and representation of monsoon-related dynamics have been identified as a key source of uncertainty in predictions at a range of temporal scales (George et al. 2016; Chen et al. 2020).

Ocean dynamics and air-sea interaction in the Bay of Bengal (BoB; Fig. 1) influence the temperature and salinity structure of the upper ocean, and so exert a crucial control on the progression of the southwest monsoon. Unlike the neighbouring Arabian Sea, which undergoes pronounced surface cooling during monsoon onset, sea surface temperature (SST) in the BoB generally remains in excess of 28°C (Shenoi et al. 2002). Above an SST threshold of 26 to 28°C, deep atmospheric convection is sustained: this heats the upper troposphere, helps sustain monsoon winds (Shenoi et al. 2002; Joseph et al. 2005), and promotes the formation of monsoon depressions, the low-pressure weather systems that commonly originate over the BoB (Goswami 1987; Hurley and Boos 2015).

Pronounced meridional and zonal property gradients in both the atmosphere and the ocean are characteristic of the BoB. SST gradients arise because of the BoB cold pool, a region of relatively low SSTs (approximately 27 to 28°C) to the east of Sri Lanka (Fig. 2a; Joseph et al. 2005; Das et al. 2016; Vinayachandran et al. 2020). The cold pool has been attributed to: (1) air-sea fluxes (Das et al. 2016); (2) the arrival of clouds from elsewhere in the Indian Ocean (Das et al. 2016; Vinayachandran et al. 2020); (3) wind-driven cooling (Vecchi and Harrison 2002); (4) open-ocean upwelling within the cold pool (Vinayachandran and Yamagata 1998; Joseph et al. 2005; Rao et al. 2006); and (5) the advection of cool, upwelled water by the Southwest Monsoon Current (SMC; Vinayachandran et al. 2020), a strong, surface-intensified current that flows northeastward into the BoB during the southwest monsoon (Vinayachan-

Corresponding author: Peter Sheehan, p.sheehan@uea.ac.uk

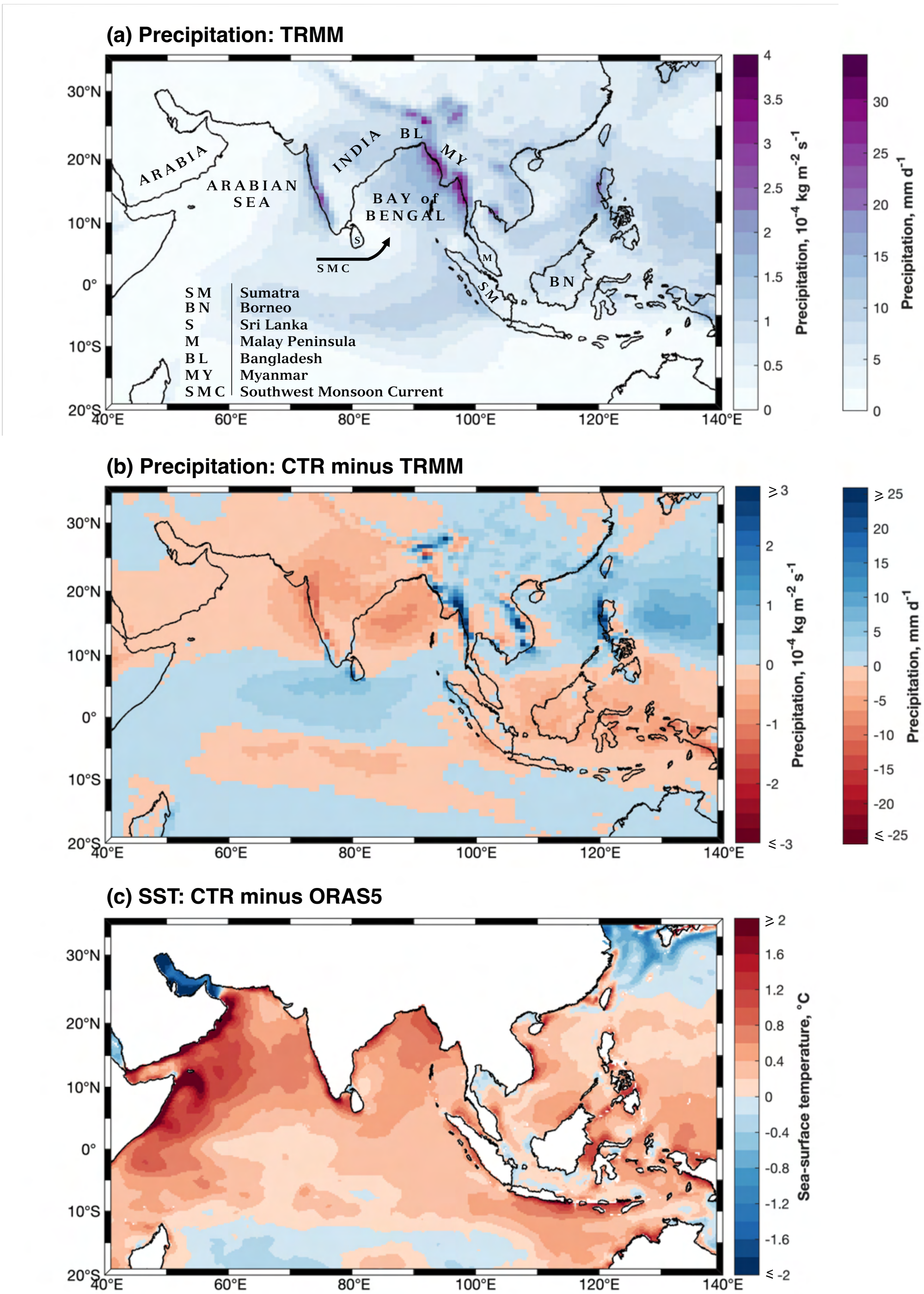

FIG. 1. **(a)** Observed JJAS mean (1998 to 2019, inclusive) precipitation from TRMM (kg m^{-2} s^{-1}; a scale in mm day^{-1} is shown for comparison). The black arrow shows the approximate path of the Southwest Monsoon Current. **(b)** The difference between JJAS mean precipitation in the control simulation (**CTR**) and TRMM (kg m^{-2} s^{-1} and mm day^{-1}). **(c)** The difference between JJAS mean sea-surface temperature in the control simulation (**CTR**) and ORAS5 (°C).

dran et al. 1999). Once established, the BoB cold pool inhibits convection, cloud formation and rainfall immediately overhead (Nair et al. 2011). The meridional SST gradient between the cold pool and the warmer waters to the north strongly influences convection and rainfall over the BoB: Shankar et al. (2007) report that intensified convection over the BoB occurs within a week of an intensified SST gradient; when the meridional temperature gradient is weaker, rainfall tends to be short lived. In contrast, relatively little is known about the impact of the zonal SST gradient on southwest monsoon rainfall.

Surface salinities in the BoB are relatively low, a consequence of the large amount of freshwater delivered both directly, via rainfall over the ocean, and indirectly, via the large, monsoon-fed river systems of the surrounding continent: the Ganges, the Brahmaputra and the Irrawaddy (Jana et al. 2015). The effect of this freshwater flux, which is particularly pronounced in the northern BoB (Vinayachandran and Kurian 2007; Jana et al. 2015), is to create strong salinity stratification in the surface layers. This stratification is accentuated by the presence of saline Arabian Sea High-Salinity Water (ASHSW) just below the surface (Jain et al. 2017), a core of which enters the BoB each year with the SMC, as has been determined from observations (Vinayachandran et al. 2013; Webber et al. 2018) and from re-analysis products (Sanchez-Franks et al. 2019). The ASHSW layer, which deepens northward into the BoB (Vinayachandran et al. 2013) forms a pronounced salinity maximum, below which salinity decreases gradually. The high-salinity core of the SMC balances the freshwater input to the BoB and therefore has considerable downstream influence over the entire basin (Vinayachandran et al. 2013). The presence of a high-salinity, near-surface layer strongly influences local profiles of mixing (George et al. 2019) and stratification (Webber et al. 2018) and thus may influence SST along its path (Webber et al. 2018).

The unusually strong salinity stratification in the BoB modifies the structure of the mixed layer, separating the halocline from the thermocline. A fresh, shallow layer of near-constant temperature and salinity lies at the very surface of the ocean and descends as far as a halocline; beneath this, temperature remains fairly constant to the depth of the main thermocline, even as salinity increases towards the ASHSW salinity maximum (George et al. 2019). The upper BoB can therefore be divided into two vertical layers, the upper of which is the true mixed layer and the lower of which, between the halocline and thermocline, is the barrier layer (Sprintall and Tomczak 1992). Together, the mixed layer and barrier layer form the isothermal layer. Barrier layers with characteristic thicknesses of between 20 and 30 m are found throughout the tropical ocean (Sprintall and Tomczak 1992; de Boyer Montégut et al. 2007; Vissa et al. 2013), but they are particularly pronounced in the BoB, where they reach thicknesses of 50 m (de Boyer Montégut et al. 2007). Barrier layers play a key role in regulating air-sea interaction in the BoB, quickening the ocean response to atmospheric forcing (Shenoi et al. 2002). They limit the penetration of surface forcing in the ocean (Shenoi et al. 2002); they often elevate SSTs by inhibiting processes such as the upward mixing of cool water (Shenoi et al. 2002); and they modulate the development of tropical cyclones (Yan et al. 2017).

In this study, we use a configuration of the Met Office Unified Model coupled to an ocean surface mixed-layer model to investigate the influence of: (1) the zonal SST gradient; (2) the meridional SST gradient; (3) and surface salinity stratification on rainfall of the South Asian monsoon. By running four multi-decadal simulations with the same model, we compare the relative effect of the meridional and zonal SST gradients, as well as surface salinity, on rainfall during the southwest monsoon. We describe the model set up and our methods and give an outline of the control simulation in Section 2. We present and discuss the results of the SST simulations in Section 3 and the salinity simulations in Section 4. We present our conclusions in Section 5.

2. Model and methods

a. Model description

We use the Global Ocean Mixed Layer 3.0 configuration of the Met Office's Unified Model (MetUM-GOML 3.0). MetUM-GOML 3.0 comprises the Multi-Column K Profile Parameterisation ocean (MC-KPP version 1.2) coupled to the MetUM Global Atmosphere 7.0 (Walters et al. 2019). The atmospheric model has a horizontal resolution of N216 (i.e. 0.56° latitude by 0.83° longitude), which corresponds to a horizontal grid spacing of approximately 90 km in the tropics. There are 85 vertical levels in the atmosphere, with approximately 50 vertical levels in the troposphere; output is provided on 17 levels, from 1000 to 10 hPa. MetUM-GOML 3.0 is configured similarly to MetUM-GOML 1.0 (Hirons et al. 2015) and MetUM-GOML 2.0 (e.g. Peatman and Klingaman 2018), except that the atmospheric model is updated to Global Atmosphere 7.0 and the air-sea coupling routines are updated to couple the models via the Ocean-Atmosphere-Sea Ice-Soil Model Coupling Toolkit (Valcke 2013). Atmospheric boundary conditions are described in detail in Walters et al. (2019).

MC-KPP consists of a grid of independent one-dimensional columns, with one column under each atmospheric grid point. Ocean columns are 1000 m deep; they have 100 vertical levels, with 70 levels in the top 300 m and a near-surface resolution of approximately 1 m. This allows an accurate representation of mixed-layer depth and SST. Ocean columns are subject to surface forcing from freshwater, heat and momentum fluxes; vertical mixing is parameterised using the KPP scheme from Large et al. (1994).

There is no explicit horizontal or vertical advection included in MC-KPP. Temperature and salinity tendency terms are added to mimic the effects of climatological temperature and salinity advection, and to account for bias in atmospheric surface fluxes. These tendency terms are calculated relative to the 1980–2009 climatology of Smith and Murphy (2007); see Hirons et al. (2015) and Peatman and Klingaman (2018) for more information on this technique. The absence of ocean dynamics means MetUM-GOML cannot represent coupled modes of variability (e.g. El Niño–Southern Oscillation, Indian Ocean Dipole) that rely on a dynamical ocean (Hirons et al. 2015). The benefit of not representing these modes of variability is that the mean signal from the perturbation simulations will not be obscured by such interannual climate variations.

When analysing simulated precipitation patterns, we consider the vertically integrated moisture flux (VIMF), $\boldsymbol{F} = (F_x, F_y)$:

$$F_x = \frac{1}{g}\int uq\,dp, \quad F_y = \frac{1}{g}\int vq\,dp. \tag{1}$$

where $g = 9.81$ m s^{-2} is the acceleration due to gravity, u and v are the zonal and meridional wind components (both m s^{-1}), q is specific humidity, and p is pressure (hPa). We integrate over all 17 pressure levels, i.e. 1000 to 10 hPa. The vertically integrated moisture equation can be written as:

$$\frac{\partial < q >}{\partial t} = -\nabla_H.\boldsymbol{F} - (P - E), \tag{2}$$

where <> denotes a vertical integral, t is time, P is precipitation, E is evaporation, and ∇_H is the horizontal differential operator. All terms in Eqn. 2 are mass fluxes of moisture with units of kg m^{-2} s^{-1}. On the timescales considered here, the change in specific humidity (atmospheric moisture storage) is negligible, so that VIMF convergence ($-\nabla_H.\boldsymbol{F}$) and $P - E$ balance. We calculate VIMF convergence, and smooth it via spectral truncation (at total wavenumber $N = 126$), using the windspharm Python library (Dawson 2016). We refer to VIMF convergence rather than the more usual VIMF divergence so that precipitation and processes contributing to precipitation are all positive in magnitude and may be plotted on the same axis.

All simulations were spun-up for one year (the output for which was discarded) and then run for 30 years. We here work with monthly mean output. The majority of our analysis is conducted on climatological averages of the southwest monsoon season (i.e. June to September; "JJAS mean" hearafter). We first calculate the JJAS-mean of a given variable for each of the 30 years of our simulations; we then calculate a single climatological JJAS mean over all 30 years. We assess the statistical significance of our results – i.e. of the difference between the control simulation and a given perturbation simulation – using a Student's t-test with a 90% significance level. This test is done using the climatological 30-year JJAS mean and its associated standard deviation.

b. Control simulation

The control simulation (**CTR**) reproduces the key features of the southwest monsoon (Figs. 1 and 2). Upper-level winds are westward over the Arabian Sea, India and the BoB (Fig. 2e); VIMF, which is dominated by low-level winds, exhibits the classic monsoonal pattern, with northward flow along the eastern coast of Africa and then eastward flow over India and the BoB (Fig. 2f). Pronounced rainfall occurs along the eastern coast of the BoB and along the southwestern coast of India (> 4 kg m^{-2} s^{-1}; Fig. 2b). A broad region of more moderate rainfall is located in east-central India, and over the equatorial Indian Ocean (1 kg m^{-2} s^{-1}; Fig. 2b). Furthermore, **CTR** reproduces the so-called "hole in the monsoon": the region of low rainfall found to the north and east of Sri Lanka (<0.25 kg m^{-2} s^{-1}; Fig. 2b). Rainfall is generally well correlated with VIMF convergence; this is particularly apparent in regions of high rainfall (Figs. 2b and f).

Observed rainfall is taken from NASA's Tropical Rainfall Monitoring Mission (TRMM; Fig. 1; Huffman et al. 2007). Compared to TRMM, simulated rainfall over Indian is generally too low, by up to 2 kg m^{-2} s^{-1} over the southwestern coast (Fig. 1b). In **CTR**, the region of moderate rainfall in east-central India does not extend far enough westward: in the observations, it extends from the eastern to the western coast of India, albeit with higher rainfall in the east (Fig. 1b). In contrast, too much rain falls along the eastern coast of the BoB: rainfall rates here are up to twice what they are in TRMM (Fig. 1b).

A monsoonal dry bias over India, which in **CTR** is 32% of observed JJAS-mean rainfall (approximately 3 to 4 mm day^{-1}; Fig. 1b), is a known limitation of the MetUM (e.g. Walters et al. 2017; Peatman and Klingaman 2018; Keane et al. 2019, 2021; Liu et al. 2021), as indeed it is a known limitation of many climate models (e.g. Goswami et al. 2014; Saha et al. 2014; Samanta et al. 2018; Wang et al. 2020; Doblas-Reyes et al. 2021; Liu et al. 2021). In CMIP6 models, over northern India there is an ensemble-mean, annual-mean dry bias of 3 to 4 mm day^{-1}; over southern India there is an ensemble-mean, annual-mean wet bias of a similar magnitude (Doblas-Reyes et al. 2021). These annual-mean biases are comparable to JJAS-mean biases (Wang et al. 2020).

In the MetUM, Keane et al. (2019) attribute the dry bias to unrealistically weak moisture-carrying winds over the Arabian Sea and to an anticyclonic bias over eastern India and the BoB (particularly pronounced in their simulation; they further suggest that this anticyclonic bias points to errors in the simulation of low-pressure systems originating

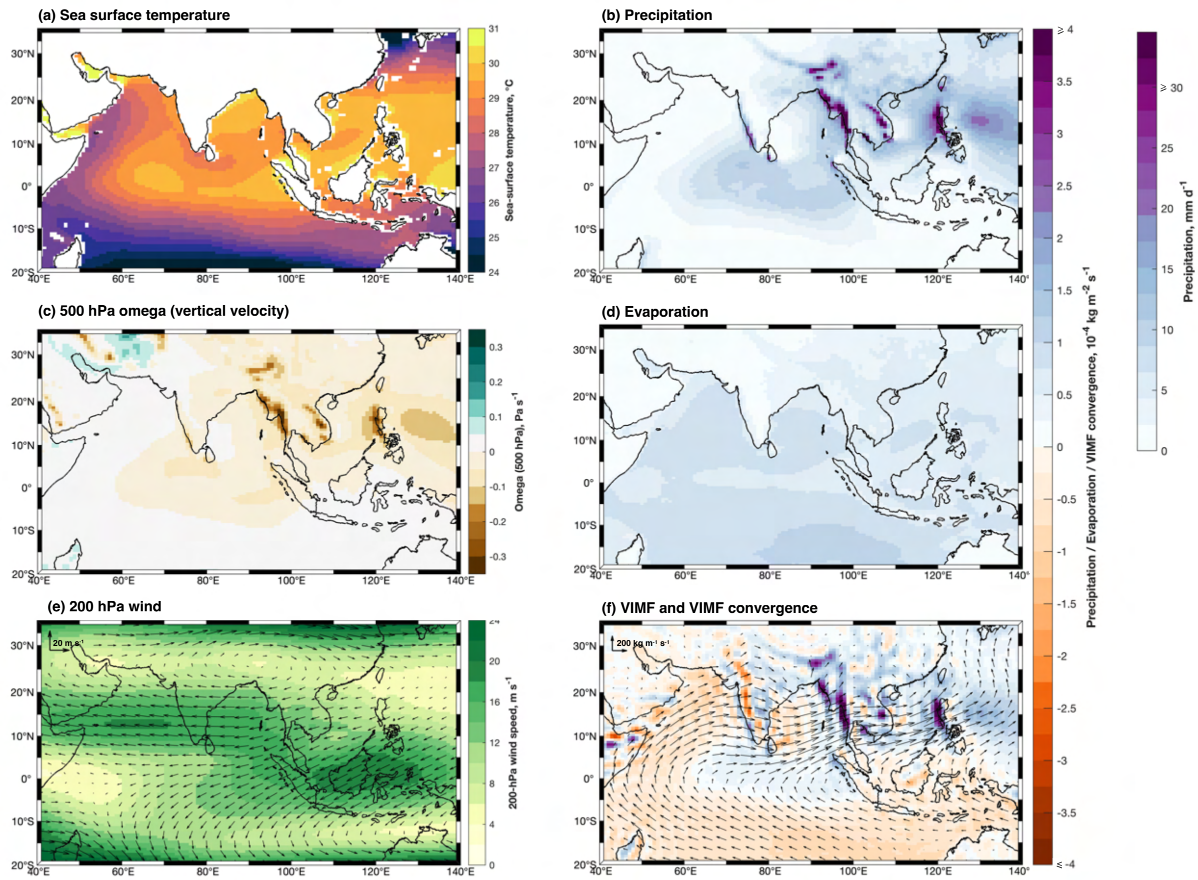

Fig. 2. JJAS climatological mean fields from the control simulation (**CTR**): **(a)** sea-surface temperature (°C); **(b)** precipitation (kg m^{-2} s^{-1}; a scale in mm day^{-1} is shown for comparison); **(c)** 500 hPa omega, i.e. vertical velocity in pressure co-ordinates (Pa s^{-1}; negative for ascent); **(d)** evaporation (kg m^{-2} s^{-1}); **(e)** 200 hPa wind (vectors) and 200 hPa wind speed (shading; both m s^{-1}); **(f)** VIMF (vectors; kg m^{-1} s^{-1}) and VIMF convergence (shading; kg m^{-2} s^{-1}). For clarity, vectors are plotted at every other grid point in latitude and longitude.

over the BoB and an attendant bias in the eastward moisture flux (i.e., it is too great). Using another model, Samanta et al. (2018) find that errors in the simulation of these low-pressure systems, which they attribute to biases in the narrow SST gradient along the eastern coast of India, are a key reason for the monsoonal dry bias over India. We note that, compared to earlier versions of MetUM-GOML, the dry bias is much improved in version 7.0 of the atmospheric model used in this study (Walters et al. 2019); this is in line with improvements in the simulation of the South Asian monsoon between CMIP5 and CMIP6 (Doblas-Reyes et al. 2021). Despite errors potentially arising from erroneous simulation of BoB low-pressure systems, the MetUM is considered to be one of the models in which these key features are better represented (Deoras et al. 2022).

SST observations are taken from the ECMWF Ocean ReAnalysis System 5 (ORAS5; Zuo et al. 2019). Simulated SST distribution in **CTR** compares favourably to ORAS5, although **CTR** SSTs are too high (by approximately 0 to 0.6°C) across the northern Indian Ocean, with the notable exception of the Persian Gulf, which is too cold (Fig. 1c). The magnitude of the warm bias generally decreases eastward with distance from Africa; the greatest warm biases are found in the western Indian Ocean and the Arabian Sea (Fig. 1c). In the BoB, the coastal SST gradient along the eastern coast of India that was identified by Samanta et al. (2018) is present, and is stronger in **CTR** than in ORAS5. More widely, the BoB's zonal SST gradient – SSTs are higher in the west than in the east, in **CTR** (Fig. 2a) as in the observations (not shown) – is weaker in **CTR** than in the observations (Fig. 1c). Given that one of our experiments involves removing the zonal SST gradient in the BoB (described in Sec. c, below), we expect that the model may underestimate the influence of this gradient on rainfall patterns and monsoon dynamics.

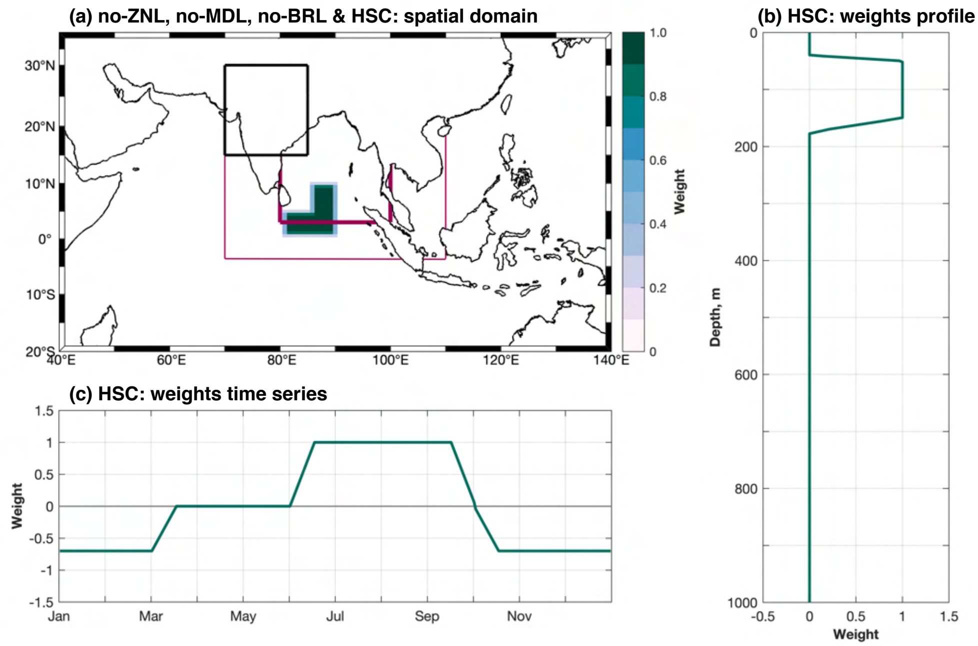

FIG. 3. **(a)** Shading indicates area over which salinity tendencies in the high-salinity core simulation (**HSC**) were applied, and the associated weighting. The thick purple line demarcates the domain within which SST is averaged in the **no-ZNL** and **no-MDL** simulations, and within which barrier layers are removed in **no-BRL**; the thin purple line demarcates the outer limit of the smoothed boundary. The black box demarcates the target region used in the moisture-tracking experiments. **(b)** Depth profile of weights applied to the additional salinity tendencies in **HSC**. **(c)** Time series of weights applied to the additional salinity tendencies in the **HSC**.

c. Sea surface temperature perturbation simulations

We run two perturbation simulations in which we modify SST in the BoB. In the first, we remove the zonal SST gradient (**no-ZNL** simulation) and in the second we remove the meridional SST gradient (**no-MDL** simulation). In each, SST was averaged (zonally or meridionally) in the BoB north of 3 °N, and between 80 and 100°E (delineated by the thick purple line in Fig. 3a). This region encompasses the SST gradients set up by the dynamics and processes introduced above (Sec. 1). Inside this region, the MC-KPP SST was averaged at each coupling timestep (1 hour) before being passed to the atmosphere. Importantly, this averaged SST was computed from the full, horizontally varying MC-KPP SST. The averaged SST was not stored or allowed to overwrite the MC-KPP SST. The averaged SST is used only in the computation of the atmospheric surface fluxes. Even these are only partially horizontally smoothed, however, as the atmospheric boundary-layer temperature and moisture remain spatially varying. The temperature (and salinity) tendency terms in MC-KPP also retain their horizontal variations. Thus, the averaged SST is computed from an SST that has evolved in response to horizontally varying atmospheric forcing and climatological oceanic advection. It is not a prescribed boundary condition. Around this smoothed region, there was a 12-gridpoint region in each direction (approximately 6.7° latitude and 10° longitude; delineated by the thin purple line in Fig. 3a) in which the smoothed and un-smoothed SST fields were linearly combined, with linearly decreasing weight away from the smoothing region, to prevent sharp SST gradients.

To identify the source regions of precipitation over northern India, we use the WAM-2layers moisture-tracking model of van der Ent et al. (2013, 2014), used recently by Guo et al. (2019, 2020) for studies of the East Asian monsoon. It is based on the atmospheric water conservation equation; it uses precipitation, evaporation, atmospheric circulation and moisture content to determine the geographical source of rain falling in a given region. WAM-2layers is integrated backwards using MetUM output (**CTR**, **no-ZNL** and **no-MDL**) from June, July, August and September to determine the amount of evaporation at each horizontal grid point that contributes to precipitation over a target region in central and northern India (70–85°E, 15–30°N; Fig. 3a); this region encompasses some of the most densely populated parts of South Asia. Simply put, WAM-2layers shows where precipitation falling over a given area last evaporated. Differences between the WAM-2layers results for, for instance, **CTR** and **no-ZNL** show whether the addition of the zonal SST gradient in the

BoB alters the source region for rainfall destined for the target region.

d. Salinity perturbation simulations

We conduct two further perturbation simulations, in which we modify the upper-ocean salinity distribution. In the first of these simulations, having noted that evidence of SMC-related salt convergence is lacking in **CTR** (not shown), we alter the model ocean's salinity tendencies to mimic the affect of the SMC's high-salinity core on local salt convergence (**HSC** simulation). Using the NEMO 1/12° ocean re-analysis (www.marine.copernicus.eu), we determine that the characteristic salt convergence (i.e. positive salinity tendency) in the SMC, α, is 0.02 g kg^{-1} day^{-1}.

During the southwest monsoon, we add this SMC salinity tendency to the **CTR** salinity tendency over a reverse L-shaped region that gives a schematic representation of the location of the SMC (Figs. 1 and 3a). The approximate location of the SMC has been established from in situ observations (Vinayachandran et al. 2013; Webber et al. 2018), satellite observations (Webber et al. 2018; Sanchez-Franks et al. 2019), and re-analysis products (Webber et al. 2018). As with **no-ZNL** and **no-MDL**, we apply a smoothing at the boundaries of the SMC in space, both horizontally and vertically; we also apply a smoothing in time. Thus, the SMC's salinity tendency, dS/dt, added at each grid point and at each time step may be represented as the product of α and three weighting functions:

$$\left.\frac{dS}{dt}\right|_{HSC} = \alpha\, f(x,y)\, g(z)\, h(t), \tag{3}$$

where $0 \leqslant f(x,y) \leqslant 1$ is the horizontal weighting function (Fig. 3a), $0 \leqslant g(z) \leqslant 1$ is the vertical weighting function (Fig. 3b), and $h(t)$ is the temporal weighting function (Fig. 3c). Note $h(t)$ is negative for three months after the southwest monsoon such that the net change in salinity is zero when integrated over a year (Fig. 3c); it is zero in April to avoid sharp tendency changes prior to the onset of the southwest monsoon.

In the second salinity perturbation simulation, we remove the barrier layer by replacing, at every timestep, the salinity profile over the depth of the isothermal layer with the average salinity of the isothermal layer (**no-BRL** simulation). Following Kara et al. (2000), we define the isothermal layer depth as the depth at which temperature is 0.5 °C lower than at a reference depth of 10 m; we define mixed layer depth as the depth at which the density is reduced by an amount equivalent to a 0.5°C reduction in temperature, assuming constant salinity. The barrier layer thickness is then the difference between these two depths. In **CTR**, barrier layers are found east of 90°E during the southwest monsoon (Fig. 4). Barrier layers were removed in the BoB north of 3°N, and between 80 and 100°E (Fig. 3a): i.e. the same region over which SST was averaged in the **no-ZNL** and **no-MDL** simulations.

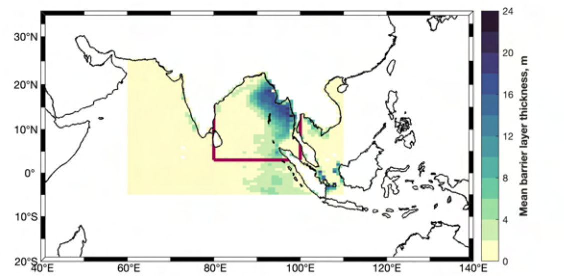

Fig. 4. JJAS climatological mean barrier layer thickness in the control simulation (**CTR**). In the no-barrier layer simulation (**BRL**), barrier layers were successfully removed, i.e. salinity was averaged over the barrier layer thickness, within the purple box.

As with **no-ZNL** and **no-MDL**, **no-BRL** is a process-denial simulation and we want to consider the impact of adding in barrier layers. Hence, the results of **no-BRL** are presented as control minus perturbation (i.e. **CTR** − **no-BRL**). In **HSC**, however, we are adding features to the perturbation experiment that are not present in **CTR** due to the smooth nature of the Smith and Murphy (2007) climatology. Hence, we do the subtraction the other way around (i.e. perturbation minus control), again to produce a difference plot that shows the effect of adding in the high-salinity core. The results of both salinity perturbation simulations are also considered as monsoon season means. The five simulations are summarised in Table 1.

3. SST gradient simulations

a. ***no-ZNL****: no zonal SST gradient*

The addition of the zonal SST gradient (**CTR**−**no-ZNL**) is associated, at a given latitude, with warmer SSTs in the western BoB and cooler SSTs in the eastern BoB (Fig. 5a). South and southwest of Sri Lanka, this pattern is reversed, with warmer SSTs in the eastern BoB between approximately 0 and 8°N (Fig. 5a). Consequently, the addition of the zonal SST gradient is associated with cooler SSTs in the western BoB and warmer SSTs in the eastern BoB at a given latitude. This reversal of the zonal SST gradient

Table 1. Summary of model simulations.

Simulation	Details
CTR	Control
no-ZNL	Zonal SST gradient removed
no-MDL	Meridional SST gradient removed
HSC	High-salinity core added
no-BRL	Barrier layer removed

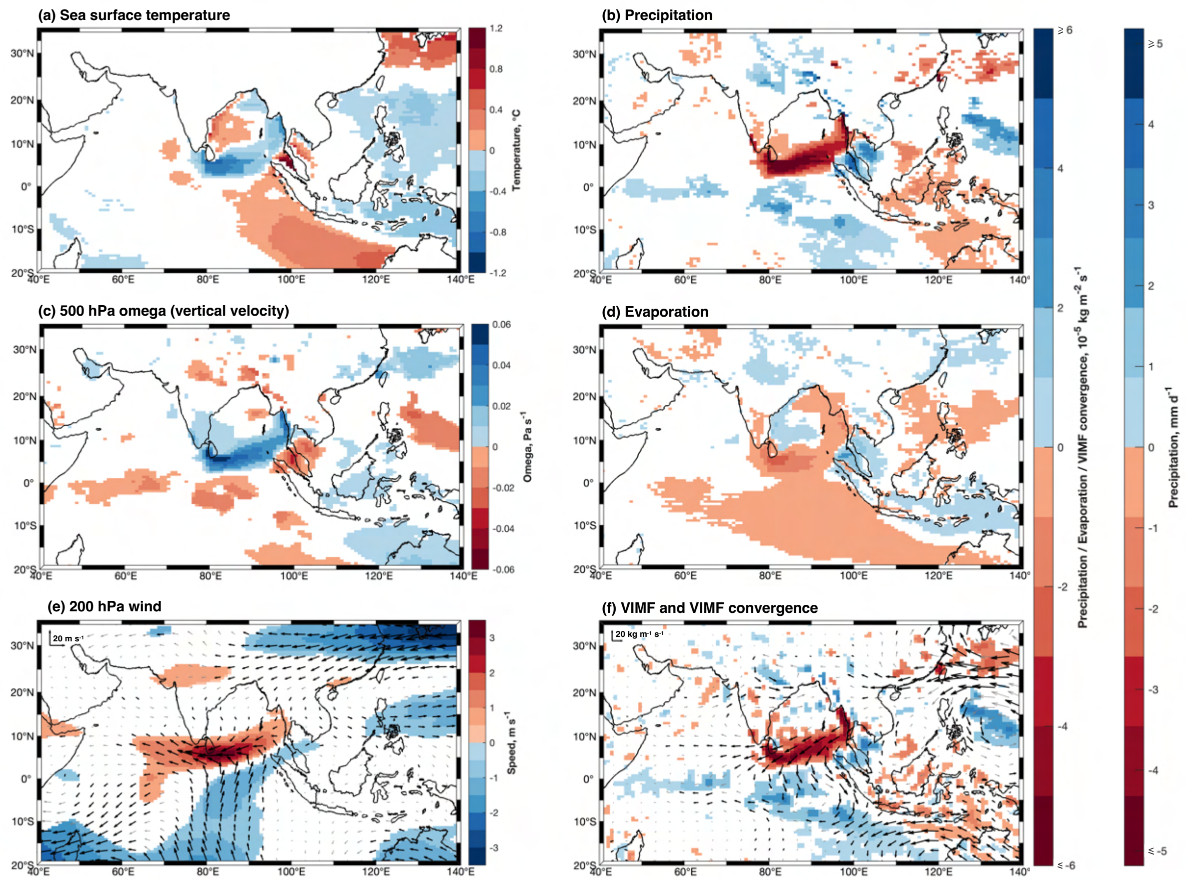

FIG. 5. Difference between JJAS climatological mean fields in the control and the no-zonal gradient simulations, i.e. **CTR – no-ZNL**, hence plots show the impact of adding the zonal gradient: **(a)** sea-surface temperature (°C); **(b)** precipitation (kg m^{-2} s^{-1}; a scale in mm day^{-1} is shown for comparison); **(c)** 500 hPa omega, i.e. vertical velocity in pressure co-ordinates (Pa s^{-1}); **(d)** evaporation (kg m^{-2} s^{-1}); **(e)** 200 hPa wind (vectors) and 200 hPa wind speed (shading; both m s^{-1}); **(f)** VIMF (vectors; kg m^{-1} s^{-1}) and VIMF convergence (shading; kg m^{-2} s^{-1}). Differences are plotted where significant at the 90% level; vectors are plotted in bold black if either component is significant at the 90% level, and in thin grey otherwise. For clarity, vectors are plotted at every other grid point in latitude and longitude.

at approximately 8°N induces a meridional SST gradient in the western BoB (Fig. 5a). Remote changes in SST are also observed outside the BoB in the eastern Indian Ocean and western Pacific Ocean (Fig 5a).

The addition of the zonal SST gradient leads to a large reduction (-6×10^{-5} kg m^{-2} s^{-1}) in precipitation over the southern BoB (Fig. 5b). This is a representative 50% reduction relative to **no-ZNL**, i.e. to when the zonal SST gradient is absent; subsequent parenthetical percentages also indicate representative relative changes from either **no-ZNL** or **no-MDL**. This reduction occurs over the region of the strongest SST decrease (Fig. 5a) and is related to a combination of reduced evaporation (Fig. 5d) and a decrease in VIMF convergence (Fig. 5f). The region of SST increase either side of the southern Malay Peninsula is co-located with a large increase in precipitation (6×10^{-5} kg m^{-2} s^{-1}; 150%; Fig. 5b) that is related to an increase in both evaporation (Fig. 5d) and VIMF convergence (Fig. 5f).

Further to the prominent reduction in precipitation over the southern BoB, the addition of the zonal SST gradient reduces precipitation over the western coast of Mayanmar and over south-central and southwestern India (Fig. 5b). The reduced precipitation over the western coast of the Malay Peninsula is related both to a decrease in evaporation (Fig. 5d) and to an increased VIMF divergence (Fig. 5f). In the presence of the zonal SST gradient, there is anomalous extraction of moisture from over the Malay Peninsula and anomalous VIMF transport westward across the southern BoB (Fig. 5f), counter to the mean VIMF (Fig. 2f). This anomalous transport ends in a region of increased VIMF convergence over the equator due south of Sri Lanka (Fig. 5b). Precipitation is increased here (Fig. 5b) despite locally reduced in evaporation (Fig. 5d).

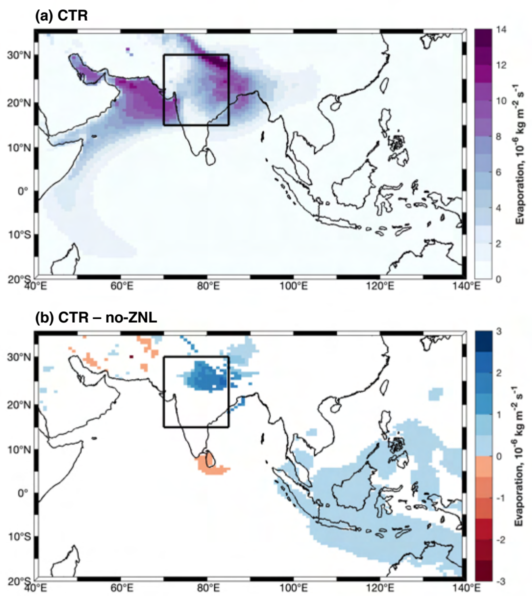

FIG. 6. **(a)** In the control simulation, **CTR**: JJAS climatological mean evaporation for precipitation falling within the black box. **(b)** Difference between JJAS climatological mean evaporation for precipitation falling within the black box **CTR** and **no-ZNL**. Differences are plotted where significant at the 90% level.

In turn, this anomalous VIMF convergence appears to be associated with weaker surface winds (10 m) in the eastern equatorial Indian Ocean (not shown). Over south-central and coastal southwestern India, the reduced precipitation is associated with locally reduced evaporation (Fig. 5d). Over coastal southwestern India, the dry anomalies are enhanced by reduced VIMF convergence (Fig. 5f).

The addition of the zonal SST gradient is associated with increased precipitation over Bangladesh and northern India (2×10^{-5} kg m^{-2} s^{-1}; 50%; Fig. 5b). Through a strengthening of the monsoonal Hadley circulation over South Asia, the pronounced SST decrease across the southern BoB leads to: anomalous descent over the SST anomaly (Fig. 5c); weak anomalous southward flow at 200 hPa (Fig. 5e); and anomalous ascent over Bangladesh and northern India (Fig. 5c). There is also an increase in 850 hPa wind speed in the region of the precipitation increase (not shown). The anomalous ascent strengthens the monsoon trough (the semi-permanent region of low surface pressure in this region during the southwest monsoon; not shown), and leads to a cyclonic VIMF anomaly (the southern branch of which, at approximately 20°N, 82°E, is significant at the 90% level) centred around a region of anomalous VIMF convergence (Fig 5f).

The influence of the anomalous ascent and VIMF convergence is seen in the moisture-tracking results, which indicate where the moisture supplying precipitation within the black box in Fig. 6 last evaporated. In **CTR**, i.e. with the BoB's zonal SST gradient, precipitation that falls within the black box comes primarily from the northern Arabian Sea, and northeastern India and Bangladesh (Fig. 6a). The addition of the zonal SST gradient increases the amount of precipitation within the black box that originates over northern India (Fig. 6b): specifically, in the same region previously identified as the locus of the anomalous ascent (Fig.5). This increase in evaporation (2×10^{-5} kg m^{-2} s^{-1}; 30%;) within the target region suggests that the increase in precipitation is a consequence of a local strengthening of the hydrological cycle, forced remotely as described above. This allows us to rule out remote processes that would increase direct moisture transport from, for instance, the Arabian Sea or BoB.

b. ***no-MDL****: no meridional SST gradient*

Precipitation anomalies that arise from the addition of the meridional SST gradient resemble those that arise from the addition of the zonal SST gradient: there is a pronounced decrease in precipitation (4 to 6×10^{-5} kg m^{-2} s^{-1}; up to 50%) over the southern BoB and over the western coast of the Malay Peninsula (Fig. 7b). This decrease in precipitation in the southern BoB occurs over the region of reduced SST (Figure 7a). The increase in SST in the northern BoB (Figure 7a) appears to have no significant net effect on local precipitation, despite the accompanying increase in local evaporation (Figure 7d), which instead contributes to the increase in rainfall downstream over Myanmar. The most pronounced precipitation changes over land are located to the east of the BoB: a reduction over the northern Malay Peninsula, and increases over the southern Malay Peninsula, northern Sumatra and much of Myanmar (Figure 7b). In the western BoB, precipitation decreases over much of Sri Lanka and over coastal regions of east-central India (Figure 7b).

Changes in precipitation in the **no-MDL** simulation resemble changes in VIMF convergence (Fig. 7b and f). Changes in VIMF itself appear to direct moisture from the northern Malay Peninsula and towards Myanmar, where there in an increase in VIMF convergence, in an anomalous anticyclonic circulation (Fig. 7f). This anticyclonic circulation anomaly, visible too in the 850 hPa wind differences (not shown), resembles that identified by Keane et al. (2019) as being partly responsible for the monsoonal dry bias in the MetUM. Our simulations suggest that this may be related to the introduction of the meridional SST gradient, as simulated by the MetUM, and thus to atmosphere-ocean interaction, in the BoB. We note that this anticyclonic anomaly does not appear in **no-ZNL**.

An increase in evaporation over the region of elevated SST in the northern BoB is counteracted by the decrease in VIMF convergence over the same region; apart from a slight decrease over parts of the northern BoB, there

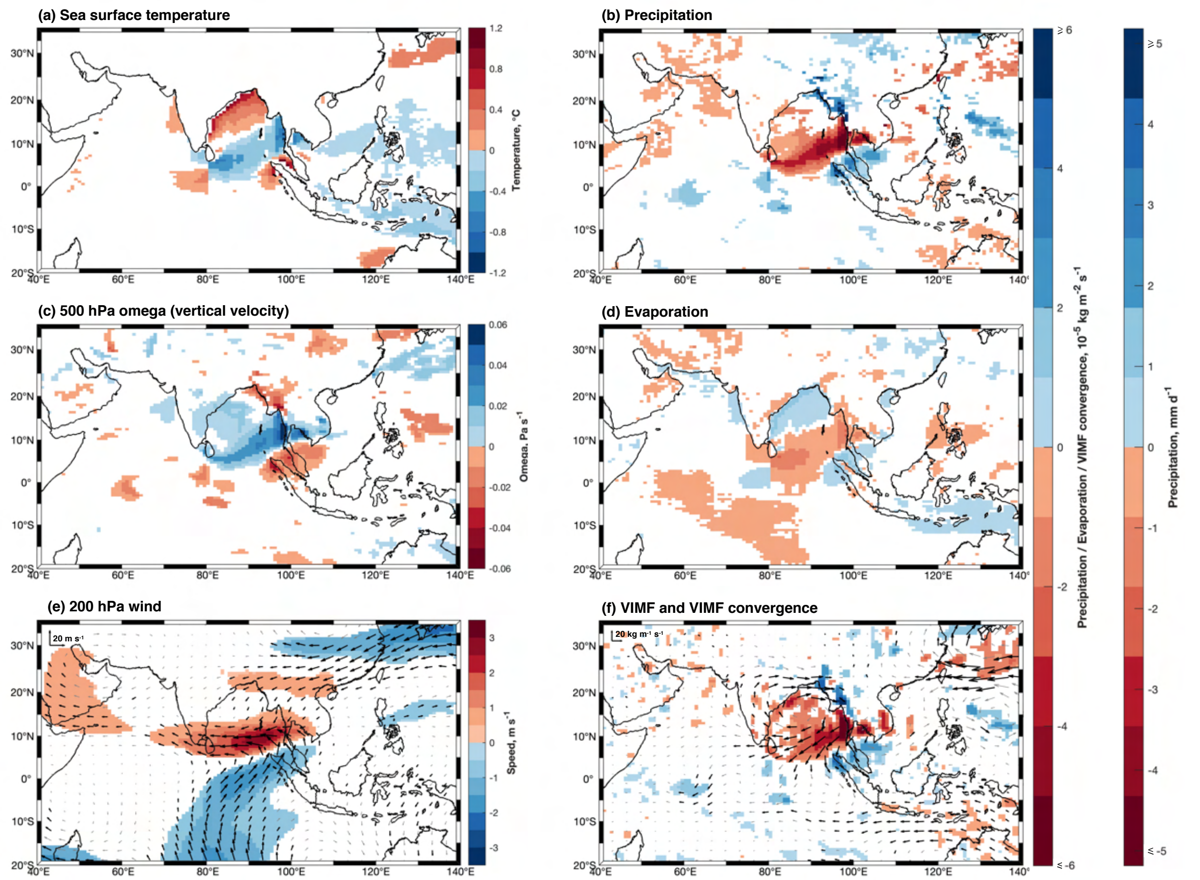

FIG. 7. Difference between JJAS climatological mean fields in the control and no-meridional gradient simulations, i.e. **CTR** – **no-MDL**, hence plots show the impact of adding the meridional gradient: **(a)** sea-surface temperature (°C); **(b)** precipitation (kg m^{-2} s^{-1}; a scale in mm day^{-1} is shown for comparison); **(c)** 500 hPa omega, i.e. vertical velocity in pressure co-ordinates (Pa s^{-1}); **(d)** evaporation (kg m^{-2} s^{-1}); **(e)** 200 hPa wind (vectors) and 200 hPa wind speed (shading; both m s^{-1}); **(f)** VIMF (vectors; kg m^{-1} s^{-1}) and VIMF convergence (shading; kg m^{-2} s^{-1}). Differences are plotted where significant at the 90% level; vectors are plotted in bold black if either component is significant at the 90% level, and in thin grey otherwise. For clarity, vectors are plotted at every other grid point in latitude and longitude.

is therefore little change in precipitation over the anomalously warm waters of the northern BoB. This result is not inconsistent with the results of Shankar et al. (2007), who find that strengthening of the meridional SST gradient ($\Delta T > 0.75$°C) occurs prior to the onset of convective rainfall over the northern BoB. We find a marginal decrease in precipitation over the northern BoB, suggesting that the complete removal of the meridional gradient may suppress precipitation. The effect appears to be small, though, and may not be as large as that following an increase above a critical threshold.

Evaporation anomalies arising from the precipitation anomalies and the corresponding changes in cloud formation are consistent with the changes in vertical velocity (Fig. 7c). Unlike in **no-ZNL**, there is no long-distance link inland areas via changes in the local Haldey cell (Fig. 7c), hence precipitation changes are generally confined to near-coastal regions (Fig. 7b).

4. Salinity stratification simulations

*a. **no-BRL**: no barrier layers*

Changes in SST and precipitation in **no-BRL** during the SW monsoon (JJAS) are generally small (Fig. 8) and are statistically significant at the 90% level in only a few regions. Furthermore, precipitation changes do not appear to be related to the region over which the perturbation forcing was applied (Fig. 3). Analysis of other variables (not shown) did not suggest a plausible mechanism behind the changes.

The influence of freshwater input and barrier layers on SST and rainfall has been the focus of previous studies. Shenoi et al. (2002) hypothesised that increases in SST

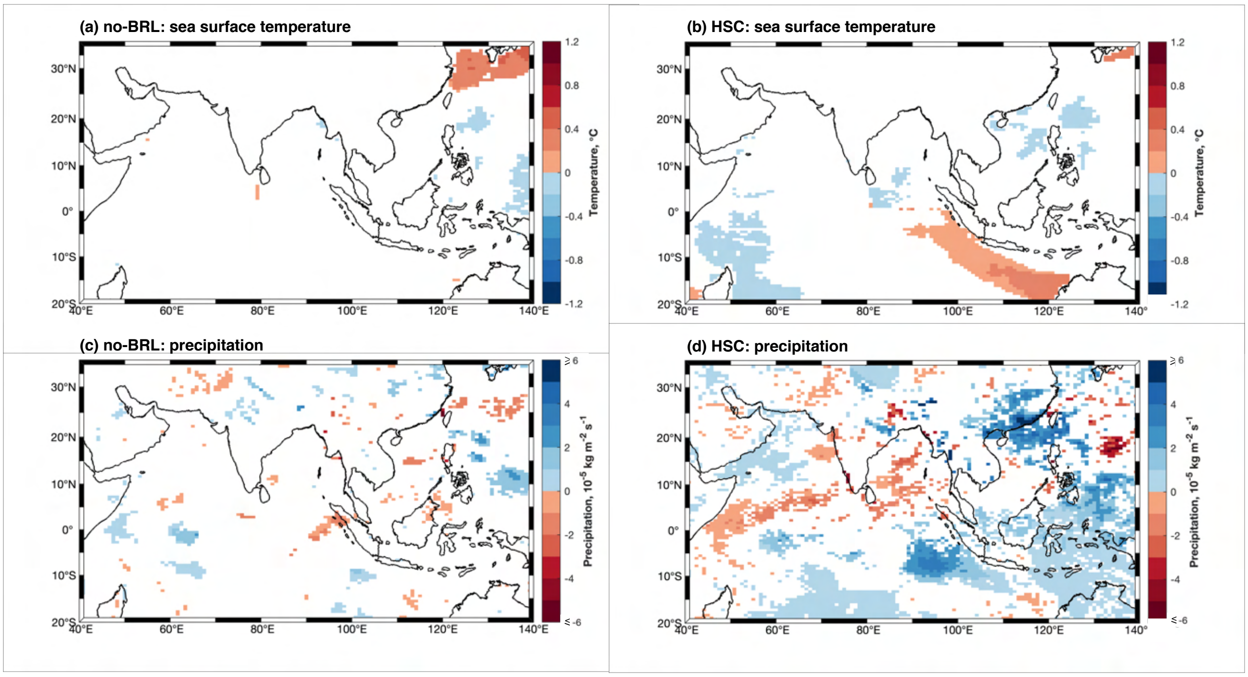

FIG. 8. Difference between JJAS climatological mean fields in the control and the no barrier layer (**CTR** – **no-BRL**; left-hand panels) simulations, and the high-salinity core and control simulations (**HSC** – **CTR**; right-hand panels). **(a)** and **(b)**, sea surface temperature differences (°C); **(c)** and **(d)**, precipitation differences (kg m^{-2} s^{-1}). Differences are plotted where significant at the 90% level. Consistent with earlier figures, positive evaporation anomalies are presented in blue.

brought about by strong salinity stratification would promote deep atmospheric convection and increase local rainfall – which, in turn, would further strengthen salinity stratification. However, Seo et al. (2009) and Krishnamohan et al. (2019) find that an increase in SST brought about by salinity stratification does not lead to significant changes in rainfall; Krishnamohan et al. (2019) add that this is because the SST increase that may be attributed to salinity stratification is offset by changes in atmospheric forcing, leading to no overall change in either SST or rainfall. Behara and Vinayachandran (2016) do not model rainfall, but they find that freshwater input, at least in parts of the BoB, shoals the mixed layer and thus increases SST, with maximum warming achieved close to river mouths.

The lack of a significant influence of the BoB's barrier layers on the rainfall of the southwest monsoon agrees with the results of Krishnamohan et al. (2019) who, contrary to the hypothesis of Shenoi et al. (2002), similarly found that removal of the barrier layer did not affect SST; in our coupled atmosphere-ocean simulation, we further confirm that this has no significant influence on SW monsoon precipitation. Explaining the lack of a change in SST, Krishnamohan et al. (2019) find that an increase in the ocean-to-atmosphere latent heat flux compensates for salinity-induced warming of the mixed layer. Furthermore, we note that the thickness and extent of barrier layers increases markedly in the months following the SW monsoon and into the northeast monsoon (November and December; Fig. 9a and b; Thadathil et al. 2007; Li et al. 2017; Kumari et al. 2018), the rainfall of the southwest monsoon being itself the principal source of freshwater to the BoB, either directly (via precipitation) or indirectly (via river run-off). Consistent with this, the **no-BRL** simulation suggests that the addition of the barrier layer drives upper-ocean changes during the northeast monsoon, which peaks in December: a shallower mixed layer raises SST by approximately 1°C in the northeastern BoB (Fig. 9d), where barrier layers are thickest, which leads to an increase in evaporation in this same region (Fig, 9f). There is no significant change in precipitation (not shown) that is linked to this increased latent heat flux. During the peak of the SW monsoon (i.e. July), barrier layers appear to be too thin, and of insufficient spatial extent, for their presence to have a significant influence on either SST or the latent heat flux (Fig. 9c and e).

*b. **HSC**: high-salinity core*

Significant changes in precipitation in **HSC** are of greater extent than in **no-BRL**, and tend to be greater in magnitude (Fig. 8). However, similar to **no-BRL**, and notwithstanding the slight SST decrease (0 to −0.2°C) over the reverse-L perturbation region (Fig. 8b), analysis of other

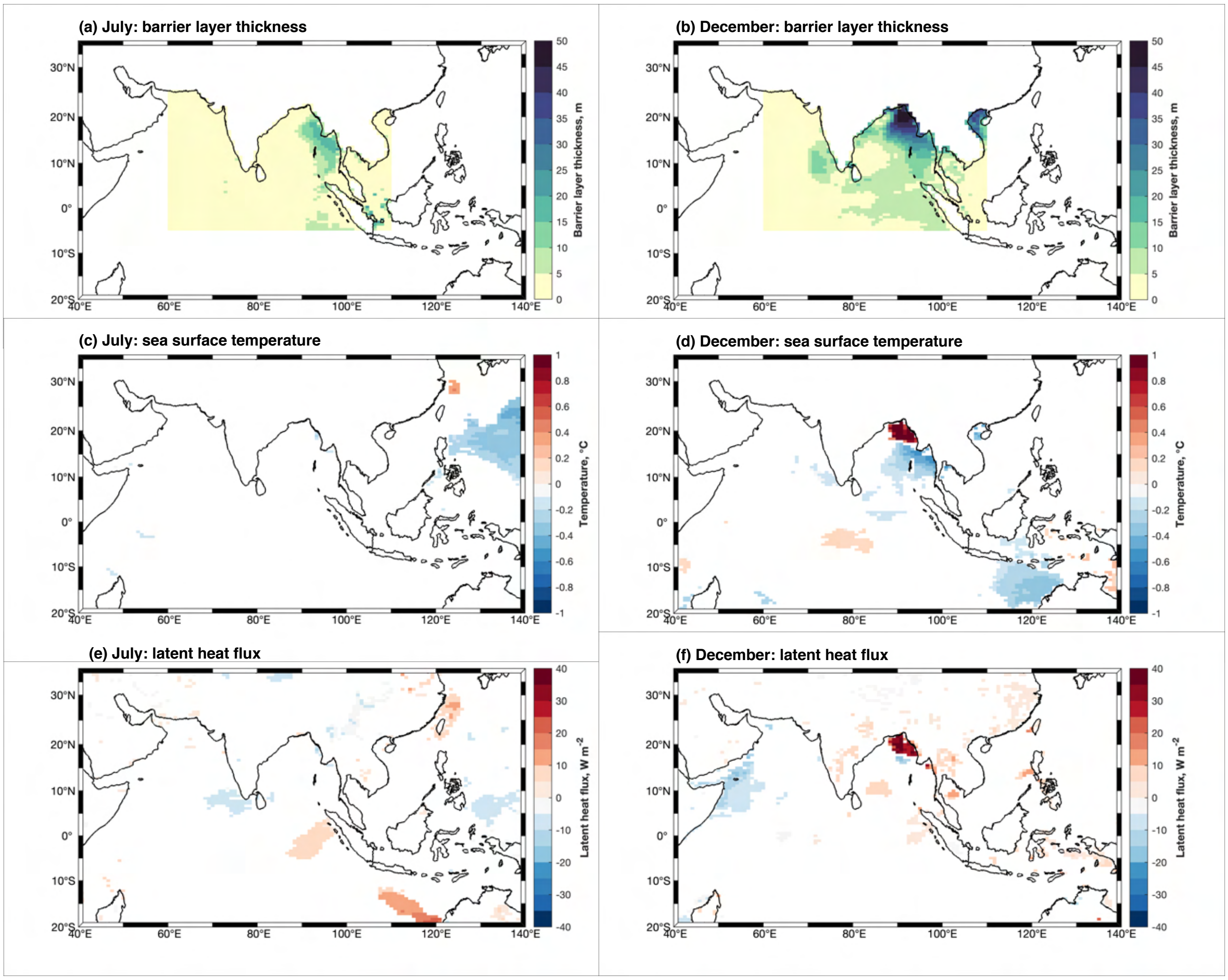

FIG. 9. Climatological mean barrier layer thickness (m) in the control simulation (**CTR**) in **(a)** July, the height of the SW monsoon and **(b)** December, the height of the NE monsoon. Difference between climatological mean sea surface temperature (°C) in the control and no-barrier layer simulations, i.e. **CTR** − **no-BRL**, in **(c)** July and **(d)** December; and difference between climatological mean evaporation (kg m^{-2} s^{-1}) in **(e)** July and **(f)** December for the same two simulations. Differences are plotted where significant at the 90% level.

variables (not shown) does not elucidate a plausible mechanism connecting the salinity perturbation with the resultant precipitation changes.

Indeed, the salinity perturbation, that is, the addition of salt at the depth of the high-salinity core during the southwest monsoon, did not have a clear influence on upper-ocean salinity in **HSC** when averaged within the reverse-L region over which the salinity perturbation was applied. Years in which upper-ocean salinity is anomalously high are almost as numerous as those in which upper-ocean salinity is anomalously low (Fig 10a). Significant salinity changes are not confined to the depth over which the perturbation was applied, being frequently greater in magnitude at the surface than at depth (Fig 10a). Furthermore, changes in stratification (i.e. buoyancy frequency) do not point to unambiguous changes caused by the addition of salt (Fig 10b), nor do they appear to match the changes in salinity itself. Stratification might be expected to change if sub-surface salinity perturbations were to induce changes to SST.

Instead, we speculate that the influence of the high-salinity core, which re-supplies the upper BoB with salt and balances the large freshwater input from the north, is felt over longer timescales than those considered in this study: that is, if the high-salinity core were somehow removed, any effect on stratification, SST and precipitation would be not be observed locally and during that same southwest monsoon, but would be observed across the basin and over the following years as the salt budget of the BoB adjusted to a new regime. This cannot be examined in MetUM-GOML given the lack of a dynamical ocean model. As the high-salinity core is a key feature of the BoB circulation

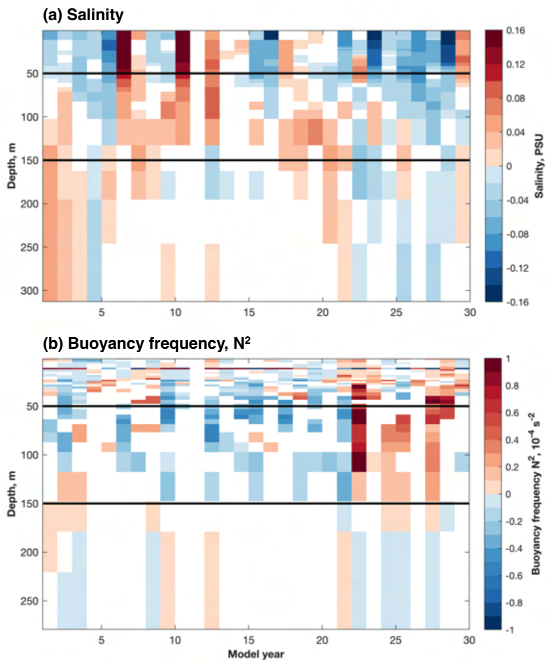

FIG. 10. Difference between JJAS climatological mean **(a)** salinity (PSU) and **(b)** buoyancy frequency (N^2; s^{-2}) in the high-salinity core and control simulations, averaged within the reverse-L region over which the salinity perturbation was applied. Difference is **HSC** − **CTR**, hence plot shows the impact of adding the high-salinity core. Differences are plotted where significant at the 90% level. The thick black lines demarcate the depth range over which the perturbation forcing was applied (Fig. 3a).

and salt budget, examining its influence in a ocean general circulation model would make an interesting topic for future research.

5. Summary and conclusions

We have reported a link between the SST gradients of the BoB and rainfall patterns of the southwest monsoon. In particular, the cooler SSTs in the southwestern BoB that give rise to the zonal SST gradient are responsible, by strengthening the local Hadley circulation, for up to 2×10^{-5} kg m^{-2} s^{-1} of rainfall over the Indo-Gangetic plain region of northern India (Fig. 5b). The meridional SST gradient also has a pronounced effect on monsoon precipitation, but does not appear to influence precipitation over land via any such remote mechanism. The addition of the high-salinity core of the SMC does not have a significant influence on monsoon rainfall in our simulations; removing the barrier layers influences rainfall, but in the months following the southwest monsoon.

Our simulations are highly idealised: for instance, the complete removal of the zonal SST gradient in the BoB is not a feature of realistic climate change projections, nor was the scenario intended to characterise any past ocean state. And furthermore, the MetUM-GOML 3.0 configuration used in this study does not allow for any remote ocean effects, nor for any dynamic ocean feedbacks. Nevertheless, using MetUM-GOML 3.0 to artificially remove an SST feature such as the BoB's zonal SST gradient allows us to examine the climatological influence of the processes that generate that SST features in the first place.

The SST gradients examined in this study are forced by a complex train of atmospheric and oceanic phenomena and are set up largely by the existence of the BoB cold pool. The cold pool, the region of relatively cool SSTs to the east of Sri Lanka (Fig. 2a), develops as open-ocean upwelling in the SMC (Vinayachandran et al. 2020) and in the Sri Lanka Dome, a cyclonic circulation feature centred on upwardly domed isotherms (Vinayachandran and Yamagata 1998; Burns et al. 2017), brings cool water to the surface. Both the SMC and the Sri Lanka Dome may be attributed to wind forcing (Vinayachandran et al. 1999; Vinayachandran and Yamagata 1998; Burns et al. 2017; Webber et al. 2018), but both are also strongly influenced, particularly towards the end of the southwest monsoon, by the arrival of westward-propagating oceanic Rossby waves (Vinayachandran and Yamagata 1998; Webber et al. 2018). These Rossby waves have themselves been excited as eastward-propagating oceanic Kelvin waves reach and interact with the Indian Ocean's eastern boundary; the propagation of Kelvin waves in particular is modulated by atmospheric phenomena such as the Madden-Julian Oscillation and the Boreal Summer Intra-seasonal Oscillation (Webber et al. 2018).

Atmospheric and oceanic dynamics, and atmosphere-ocean interaction, are key at all stages in the formation of the cold pool and hence in the genesis of the SST gradients in the BoB. The results presented above demonstrate the importance of correctly representing the dynamical processes that underlie these gradients, both for accurately modelling local monsoon rainfall patterns but also for accurately modelling monsoon rainfall over the densely populated Indo-Gangetic Plain region of northern India. Simulations that change the SST distribution that arises from these large-scale, three-dimensional dynamical features, such as the zonal SST gradient, exert a greater influence on rainfall of the southwest monsoon – and especially on rainfall over land – than do simulations that make changes to one-dimensional processes. In particular, we uncover a new mechanism by which the zonal SST gradient of the BoB, and the cold pool that sustains this zonal gradient, influences the rainfall of the southwest monsoon over northern India.

Acknowledgments. The Bay of Bengal Boundary Layer Experiment, jointly funded by the Ministry of Earth Sciences (India) and NERC/UKRI (United Kingdom), supported PMFS, BGMW and AJM (NE/L013827/1), ASF (NE/L013835/1), and PNV. NPK was supported by a

NERC Independent Research Fellowship (NE/L010976/1). Part of the research presented in this paper was carried out on the High Performance Computing Cluster supported by the Research Computing Service at the University of East Anglia. PMFS thanks Andy Heaps and Liang Guo, both of the National Centre for Atmospheric Sciences (Reading, United Kingdom) for assistance in accessing archived model output and for assistance with the WAM-2layers moisture-tracking model respectively.

Data availability statement. The code of the MetUM is available only under license from the UK Met Office; for details, see www.metoffice.gov.uk/research/modelling-systems/unified-model. Output relevant to this paper has been archived at https://figshare.com/articles/dataset/Sheehan_et_al_2022_MetUM_output/19620975. The WAM-2layers model code is available at github.com/ruudvdent/WAM2layersPython/tree/distance/.

References

Behara, A., and P. N. Vinayachandran, 2016: And OGCM study of the impact of rain and river water forcing on the Bay of Bengal. *Journal of Geophysical Research: Oceans*, **121**, 2425 – 2446.

Bombardi, R. J., V. Moron, and J. S. Goodnight, 2020: Detection, variability and predictability of monsoon onset and withdrawal dates: a review. *International Journal of Climatology*, **40**, 641 – 667.

Burns, J. M., B. Subrahmanyam, and V. S. N. Murty, 2017: On the dynamics of the Sri Lanka dome in the Bay of Bengal. *Journal of Geophysical Research: Atmospheres*, **122**, 7737 – 7750.

Chen, Z., T. Zhou, L. Zhang, X. Chen, W. Zhang, and J. Jiang, 2020: Global land monsoon precipitation changes in CMIP6 projections. *Geophysical Research Letters*.

Das, U., P. N. Vinayachandran, and A. Behara, 2016: Formation of the southern Bay of Bengal cold pool. *Climate Dynamics*, **47**, 2009 – 2023.

Dawson, A., 2016: Windspharm: a high-level library for global wind field computations using spherical harmonics. *Journal of Open Research Software*, **4**, e31.

de Boyer Montégut, C., J. Mignot, A. Lazar, and S. Cravatte, 2007: Control of salinity on the mixed layer depth in the world ocean: 1. general description. *Journal of Geophysical Research*, **112**, C06 011.

Deoras, A., A. G. Turner, and K. M. R. Hunt, 2022: The structure of strong Indian monsoon low-pressure systems in subseasonal-to-seasonal prediction models. *Quarterly Journal of the Royal Meteorological Society*, **148**, 2147 – 2166.

Doblas-Reyes, F. J., and Coauthors, 2021: Linking global to regional climate change. *Climate Change 2021: the Physical Science Basis, contribution of working group one to the Sixth Assessment Report of the Intergovernmental Panel on Climate Change*, V. Masson-Delmotte, P. Zhai, A. Pirani, S. L. Connors, C. Péan, S. Berger, N. Caud, Y. Chen, L. Goldfarb, M. I. Gomis, M. Huang, K. Leitzell, E. Lonnoy, J. B. R. Matthews, T. K. Maycock, T. Waterfield, O. Yelekçi, R. Yu, and B. Zhou, Eds., Cambridge University Press, Cambridge, United Kingdom, 1363 – 1512.

Gadgil, S., and K. Rupa Kumar, 2006: The Asian monsoon: agriculture and economy. *The Asian monsoon*, B. Wang, Ed., Springer-Verlag, Berlin, Germany.

George, G., D. N. Rao, C. T. Sabeerali, A. Srivastava, and S. A. Rao, 2016: Indian summer monsoon prediction and simulation in CFSv2 coupled model. *Atmospheric Science Letters*, **17**, 57 – 64.

George, J. V., and Coauthors, 2019: Mechanisms of barrier layer formation and erosion from in situ observations in the Bay of Bengal. *Journal of Physical Oceanography*, **49**, 1183 – 1200.

Goswami, B. B., M. Deshpande, P. Mukhopadhyay, S. K. Saha, R. Rao, S. A. Murthugudde, and B. N. Goswami, 2014: Simulation of monsoon intraseasonal variability in NCEP CFSv2 and its role on systematic bias. *Climate Dynamics*, **43**, 2725 – 2745.

Goswami, B. N., 1987: A mechanism for the west-north west movement of monsoon depressions. *Nature*, **326**, 376 – 378.

Guo, L., R. J. van der Ent, N. P. Klingaman, M.-E. Demory, P. L. Vidale, A. G. Turner, C. C. Stephan, and A. Chevuturi, 2019: Moisture sources for East Asian precipitation: mean seasonal cycle and interannual variability. *Journal of Hydrometeorology*, **20**, 657 – 672.

Guo, L., R. J. van der Ent, N. P. Klingaman, M.-E. Demory, P. M. Vidale, A. G. Turner, C. C. Stephan, and A. Chevuturi, 2020: Effects of horizontal resolution and air-sea coupling on simulated moisture source for East Asian precipitation in MetUM GA6/GC2. *Geoscientific Model Develeopment*, **13**, 6011 – 6028.

Hirons, L. C., N. P. Klingaman, and S. J. Woolnough, 2015: MetUM-GOML1: a near-globally coupled atmosphere-ocean-mixed-layer model. *Geoscientific Model Develeopment*, **8**, 363 – 379.

Huffman, G. J., and Coauthors, 2007: The TRMM Multisatellite Precipitation Analysis (TMPA): quasi-global, multi-year, combined-sensor precipitation estimates at fine scales. *Journal of Hydrometeorology*, **8**, 38 – 55.

Hurley, J. V., and W. R. Boos, 2015: A global climatology of monsoon low-pressure systems. *Quarterly Journal of the Royal Meteorological Society*, **141**, 1049 – 1064.

Jain, V., and Coauthors, 2017: Evidence for the existence of Persian Gulf Water and Red Sea Water in the Bay of Bengal. *Climate Dynamics*, **48**, 3207 – 3226.

Jana, S., A. Gangopadhyay, and A. Chakraborty, 2015: Impact of seasonal river input on the Bay of Bengal simulation. *Continental Shelf Research*, **104**, 45 – 62.

Joseph, P. V., K. P. Sooraj, C. A. Babu, and T. P. Sabin, 2005: A cold pool in the Bay of Bengal and its interaction with the active-break cycle of the monsoon. *CLIVAR Exchanges*, **10**, 10 – 12.

Kara, A. B., P. A. Rochford, and H. E. Hurlburt, 2000: An optimal definition for ocean mixed layer depth. *Journal of Geophysical Research*, **105**, 16 803 – 16 821.

Keane, R. J., D. J. Parker, and J. K. Fletcher, 2021: Biases in Indian summer monsoon precipitation forecasts in the Unified Model and their relationship with BSISO index. *Geophysical Research Letters*, **48**, e2020GL090 529.

Keane, R. J., K. D. Williams, A. J. Stirling, G. M. Martin, C. E. Birch, and D. J. Parker, 2019: Fast biases in monsoon rainfall over southern and central India in the Met Office Unified Model. *Journal of Climate*, **32**, 6385 – 6402.

Krishna Kumar, K., K. Rupa Kumar, R. G. ashrit, N. R. Deshpande, and J. W. Hansen, 2004: Climate impacts on Indian agriculture. *International Journal of Climatology*, **24**, 1375 – 1393.

Krishnamohan, K. S., and Coauthors, 2019: Is there an effect of Bay of Bengal salinity on the northern Indian Ocean climatological rainfall? *Deep-Sea Research II*.

Kumari, A., S. Prasanna Kumar, and A. Chakraborty, 2018: Seasonal and interannual variability in the barrier layer of the Bay of Bengal. *Journal of Geophysical Research: Oceans*, **123**, 1001 – 1015.

Large, W. G., J. C. McWilliams, and S. C. Doney, 1994: Oceanic vertical mixing: a review and a model with non-local boundary layer parameterisation. *Reviews of Geophysics*, **32**, 363 – 403.

Li, Y., W. Han, M. Ravichandran, W. Wang, T. Shinoda, and T. Lee, 2017: Bay of Bengal salinity stratification and Indian summer monsoon intraseasonal oscillation: 1. Intraseasonal variability and causes. *Journal of Geophysical Research: Oceans*, **122**, 4291 – 4311.

Liu, Z., M. A. Bollasina, L. J. Wilcox, J. M. Rodríguez, and L. A. Regayre, 2021: Contrasting the role of regional and remote circulation in driving Asian monsoon biases in MetUM GA7.1. *Journal of Geophysical Research: Atmospheres*, **126**, e2020JD034 342.

Nair, A. K. M., K. Rajeev, S. Sikijumar, and S. Meenu, 2011: Characteristics of a persistent "pool of inhibited cloudiness" and its genesis over the Bay of Bengal associated with the Asian summer monsoon. *Annales Geophysicae*, **29**, 1247 – 1252.

Parthasarathy, B., A. A. Munot, and D. R. Kothawale, 1994: All-India monthly and seasonal rainfall series: 1871 – 1993. *Theoretical and Applied Climatology*, **49**, 217 – 224.

Peatman, S. C., and N. P. Klingaman, 2018: The Indian summer monsoon in MetUM-GOML2.0: effects of air-sea coupling and resolution. *Geoscientific Model Develeopment*, **11**, 4693 – 4709.

Rao, R. R., M. S. Girish Kumar, M. Ravichandran, and B. K. Samala, 2006: Observed mini-cold pool off the southern tip of India and its intrusion into the south-central Bay of Bengal during the summer monsoon season. *Geophysical Research Letters*, **33**, L06 607.

Saha, S. K., A. Hazra, S. Pokhrel, H. S. Chaudhari, K. Sujith, A. Rai, H. Rahaman, and B. N. Goswami, 2019: Unravelling the mystery of Indian summer monsoon prediction: improved estimate of the predictability limit. *Journal of Geophysical Research: Atmospheres*, **124**, 1962 – 1974.

Saha, S. K., and Coauthors, 2014: Improved simulation of Indian summer monsoon in latest NCEP climate forecast system free run. *International Journal of Climatology*, **34**, 1628 – 1641.

Samanta, D., S. N. Hameed, D. Jin, T. V., M. Ganai, S. A. Rao, and M. Deshpande, 2018: Impact of a narrow coatal Bay of Bengal sea surface temperature front on an Indian summer monsoon simulation. *Scientific Reports*, **8**, 17 694.

Sanchez-Franks, A., B. G. M. Webber, B. A. King, P. N. Vinayachandran, A. J. Matthews, P. M. F. Sheehan, A. Behara, and C. P. Neema, 2019: The railroad switch effect of seasonally reversing currents on the Bay of Bengal high-salinity core. *Geophysical Research Letters*, **46**, 6005 – 6014.

Seo, H., S.-P. Xie, R. Murtugudde, M. Jochum, and A. J. Miller, 2009: Seasonal effects on Indian Ocean forcing in a regional coupled model. *Journal of Climate*, **22**, 6577 – 6596.

Shankar, D., S. R. Shetye, and P. V. Joseph, 2007: Link between convection and meridional gradient of sea surface temperature in the Bay of Bengal. *Journal of Earth System Science*, **116**, 385 – 406.

Shenoi, S. S. C., D. Shankar, and S. R. Shetye, 2002: Differences in heat budgets of the near-surface Arabian Sea and Bay of Bengal: implications for the summer monsoon. *Journal of Geophysical Research*, **107**, C6, 3052.

Smith, D. M., and J. M. Murphy, 2007: An objective ocean temperature and salinity analysis using covariances from a global climate an objective ocean temperature and salinity analysis using covariances from a global climate model. *Journal of Geophysical Research*, **112**, C02 022.

Sprintall, J., and M. Tomczak, 1992: Evidence of the barrier layer in the surface layer of the tropics. *Journal of Geophysical Research*, **97**, 7305 – 7316.

Thadathil, P., P. M. Muraleedharan, R. R. Rao, G. V. Somayajulu, Y. K. Reddy, and C. Revichandran, 2007: Observed seasonal variability of barrier layer in the Bay of Bengal. *Journal of Geophysical Research*, **112**, C02 009.

Valcke, S., 2013: The OASIS3 coupler: a European climate modelling community software. *Geoscientific Model Develeopment*, **6**, 373 – 388.

van der Ent, R. J., O. A. Tuinenburg, H.-R. Knoche, H. Kunstmann, and H. H. G. Savenije, 2013: Should we use a simple or complex model for moisture recycling and atmospheric moisture tracking? *Hydrology and Earth System Sciences*, **17**, 4869 – 4884.

van der Ent, R. J., L. Wang-Erlandsson, P. W. Keys, and H. H. G. Savenije, 2014: Contrasting roles of interception and transpiration in the hydrological cycle – part 2: Moisture recycling. *Earth System Dyanamics*, **5**, 471 – 489.

Vecchi, G. A., and D. E. Harrison, 2002: Monsoon breaks and subseasonal sea surface temperature variability in the Bay of Bengal. *Journal of Climate*, **15**, 1485 – 1493.

Vinayachandran, P. N., U. Das, D. Shankar, S. Jahfer, A. Behara, T. M. Balakrishnan Nair, and G. S. Bhat, 2020: Maintenance of the southern Bay of Bengal cold pool. *Deep-Sea Research II*.

Vinayachandran, P. N., and J. Kurian, 2007: Hydrographic observations and model simulation of the Bay of Bengal freshwater plume. *Deep-Sea Research I*, **54**, 471 – 486.

Vinayachandran, P. N., Y. Masumoto, T. Mikawa, and T. Yamagata, 1999: Intrusion of the Southwest Monsoon Current into the Bay of Bengal. *Journal of Geophysical Research*, **104**, 11 077 – 11 085.

Vinayachandran, P. N., D. Shankar, S. Vernekar, K. K. Sandeep, P. Amol, C. P. Neema, and A. Chatterjee, 2013: A summer monsoon pump to keep the Bay of Bengal salty. *Geophysical Research Letters*, **40**, 1777 – 1782.

Vinayachandran, P. N., and T. Yamagata, 1998: Monsoon response of the sea around Sri Lanka: generation of thermal domes and anticyclonjic vortices. *Journal of Physical Oceanography*, **28**, 1946 – 1960.

Vissa, N. K., A. N. V. Satyanarayana, and B. Prasad Kumar, 2013: Comparison of mixed layer depth and barrier layer thickness for the Indian Ocean using two different climatologies. *International Journal of Climatology*, **33**, 2855 – 2870.

Walters, D., and Coauthors, 2017: The Met Office Unified Model Global Atmosphere 6.0/6.1 abd JULES Global Land 6.0/6.1 configurations. *Geoscientific Model Develeopment*, **10**, 1487 – 1520.

Walters, D., and Coauthors, 2019: The Met Office UnifiedModel Global Atmosphere 7.0/7.1 and JULES Global Land 7.0 configurations. *Geoscientific Model Develeopment*, **12**, 1909 – 1963.

Wang, B., C. Jin, and J. Liu, 2020: Understanding future change of global monsoons projected by CMIP6 models. *Journal of Climate*, **33**, 6471 – 6489.

Webber, B. G. M., A. J. Matthews, P. N. Vinayachandran, C. P. Neema, A. Sanchez-Franks, V. Vijith, P. Amol, and D. B. Baranowski, 2018: The dynamics of the Southwest Monsoon Current in 2016 from high-resolution observations and models. *Journal of Physical Oceanography*, **48**, 2259 – 2282.

Yan, Y., L. Li, and C. Wang, 2017: The effects of oceanic barrier layer on the upper-ocean response to tropical cyclones. *Journal of Geophysical Research: Oceans*, **122**, 4829 – 4844.

Zhou, Z.-Q., S.-P. Xie, and R. Zhang, 2019: Variability and predictability of Indian rainfall during the monsoon onset month of June. *Geophysical Research Letters*, **46**, 14 782 – 14 788.

Zuo, H., M. Alonso Balmaseda, S. Tietsche, K. Morgensen, and M. Mayer, 2019: The ECMWF operational ensemble reanalysis-analysis system for ocean and sea ice: a description of the system and assessment. *Ocean Science*, **15**, 779 – 808.